Interband cascade laser based mid-infrared methane sensor system using a novel electrical-domain self-adaptive direct laser absorption spectroscopy (SA-DLAS)

FANG SONG,[1] CHUANTAO ZHENG,[1,2,4] WANHONG YAN, [1] WEILIN YE,[2,3] YIDING WANG,[1] AND FRANK K. TITTEL[2]

[1]*State Key Laboratory of Integrated Optoelectronics, College of Electronic Science and Engineering, Jilin University, 2699 Qianjin Street, Changchun 130012, China*
[2]*Department of Electrical and Computer Engineering, Rice University, 6100 Main Street, Houston, Texas 77005, USA*
[3]*College of Engineering, Shantou University, 243 Daxue Road, Shantou 515063, China*
[4]*zhengchuantao@jlu.edu.cn*

Abstract: To suppress sensor noise with unknown statistical properties, a novel self-adaptive direct laser absorption spectroscopy (SA-DLAS) technique was proposed by incorporating a recursive, least square (RLS) self-adaptive denoising (SAD) algorithm and a 3291 nm interband cascade laser (ICL) for methane (CH_4) detection. Background noise was suppressed by introducing an electrical-domain noise-channel and an expectation-known-based RLS SAD algorithm. Numerical simulations and measurements were carried out to validate the function of the SA-DLAS technique by imposing low-frequency, high-frequency, White-Gaussian and hybrid noise on the ICL scan signal. Sensor calibration, stability test and dynamic response measurement were performed for the SA-DLAS sensor using standard or diluted CH_4 samples. With the intrinsic sensor noise considered only, an Allan deviation of ~43.9 ppbv with a ~6 s averaging time was obtained and it was further decreased to 6.3 ppbv with a ~240 s averaging time, through the use of self-adaptive filtering (SAF). The reported SA-DLAS technique shows enhanced sensitivity compared to a DLAS sensor using a traditional sensing architecture and filtering method. Indoor and outdoor atmospheric CH_4 measurements were conducted to validate the normal operation of the reported SA-DLAS technique.

OCIS codes: (280.3420) Laser sensors; (300.6340) Spectroscopy, infrared; (140.5965) Semiconductor lasers, quantum cascade.

References and links

1. I. J. Simpson, F. S. Rowland, S. Meinardi, and D. R. Blake, "Influence of biomass burning during recent fluctuations in the slow growth of global tropospheric methane," Geophys. Res. Lett. **33**(22), L22808 (2006).
2. B. Heiko, G. F. France, G. T. Charles, R. S. Clare, J. E. Tim, M. Ian, S. Anatoly, N. Sten, S. Anatoly, O. Alexander, and S. Christiane, "Impact of the Arctic Oscillation pattern on inter-annual forest fire variability in Central Siberia," Geophys. Res. Lett. **32**, L14709 (2005).
3. N. Lang, U. Macherius, M. Wiese, H. Zimmermann, J. Röpcke, and J. H. van Helden, "Sensitive CH4 detection applying quantum cascade laser based optical feedback cavity-enhanced absorption spectroscopy," Opt. Express **24**(6), A536–A543 (2016).
4. W. Ye, C. Li, C. Zheng, N. P. Sanchez, A. K. Gluszek, A. J. Hudzikowski, L. Dong, R. J. Griffin, and F. K. Tittel, "Mid-infrared dual-gas sensor for simultaneous detection of methane and ethane using a single continuous-wave interband cascade laser," Opt. Express **24**(15), 16973–16985 (2016).
5. E. S. F. Berman, M. Fladeland, J. Liem, R. Kolyer, and M. Gupta, "Greenhouse gas analyzer for measurements of carbon dioxide, methane, and water vapor aboard an unmanned aerial vehicle," Sens. Actuators B Chem. **169**(4), 128–135 (2012).
6. A. Groth, C. Maurer, M. Reiser, and M. Kranert, "Determination of methane emission rates on a biogas plant using data from laser absorption spectrometry," Bioresour. Technol. **178**, 359–361 (2015).

7. C. T. Zheng, W. L. Ye, N. P. Sanchez, C. G. Li, L. Dong, Y. D. Wang, R. J. Griffin, and F. K. Tittel, "Development and field deployment of a mid-infrared methane sensor without pressure control using interband cascade laser absorption spectroscopy," Sens. Actuators B Chem. **244**, 365–372 (2017).

8. R. Sur, K. Sun, J. B. Jeffries, J. G. Socha, and R. K. Hanson, "Scanned-wavelength-modulation-spectroscopy sensor for CO, CO2, CH4, and H2O in a high-pressure engineering-scale transport-reactor coal gasifier," Fuel **150**, 102–111 (2015).

9. J. Jiang, G. M. Ma, H. T. Song, C. R. Li, Y. T. Luo, and H. B. Wang, "Highly sensitive detection of methane based on tunable diode laser absorption spectrum," in *Instrumentation & Measurement Technology Conference* (2016), pp. 1–5.

10. G. J. Zhang and X. L. Wu, "A novel CO2 gas analyzer based on IR absorption," Opt. Lasers Eng. **42**(2), 219–231 (2004).

11. C. T. Zheng, W. L. Ye, G. L. Li, X. Yu, C. X. Zhao, Z. W. Song, and Y. D. Wang, "Performance enhancement of a mid-infrared CH_4, detection sensor by optimizing an asymmetric ellipsoid gas-cell and reducing voltage-fluctuation: Theory, design and experiment," Sens. Actuators B Chem. **160**(1), 389–398 (2011).

12. W. Ren, L. Luo, and F. K. Tittel, "Sensitive detection of formaldehyde using an interband cascade laser near 3.6 μm," Sens. Actuators B Chem. **221**, 1062–1068 (2015).

13. M. A. Bolshov, Y. A. Kuritsyn, and Y. V. Romanovskii, "Tunable diode laser spectroscopy as a technique for combustion diagnostics," Spectrochim. Acta B At. Spectrosc. **106**, 45–66 (2015).

14. P. Werle, "A review of recent advances in semiconductor laser based gas monitors," Spectrochim. Acta A **54**(2), 197–236 (1998).

15. S. Schilt, L. Thévenaz, and P. Robert, "Wavelength modulation spectroscopy: combined frequency and intensity laser modulation," Appl. Opt. **42**(33), 6728–6738 (2003).

16. J. A. Silver, "Frequency-modulation spectroscopy for trace species detection: theory and comparison among experimental methods," Appl. Opt. **31**(6), 707–717 (1992).

17. L. Dong, C. G. Li, N. P. Sanchez, A. K. Gluszek, R. J. Griffin, and F. K. Tittel, "Compact CH_4 sensor system based on a continuous-wave, low power consumption, room temperature interband cascade laser," Appl. Phys. Lett. **108**(1), 011106 (2016).

18. L. Dong, Y. Yu, C. Li, S. So, and F. K. Tittel, "Ppb-level formaldehyde detection using a CW room-temperature interband cascade laser and a miniature dense pattern multipass gas cell," Opt. Express **23**(15), 19821–19830 (2015).

19. Y. Cao, N. P. Sanchez, W. Jiang, R. J. Griffin, F. Xie, L. C. Hughes, C. E. Zah, and F. K. Tittel, "Simultaneous atmospheric nitrous oxide, methane and water vapor detection with a single continuous wave quantum cascade laser," Opt. Express **23**(3), 2121–2132 (2015).

20. J. Li, U. Parchatka, and H. Fischer, "Development of field-deployable QCL sensor for simultaneous detection of ambient N2O and CO," Sens. Actuators B Chem. **182**, 659–667 (2013).

21. K. M. Manfred, G. A. D. Ritchie, N. Lang, J. Röpcke, and J. H. van Helden, "Optical feedback cavity-enhanced absorption spectroscopy with a 3.24 m interband cascade laser," Appl. Phys. Lett. **106**(22), 221106 (2015).

22. J. H. Northern, S. O'Hagan, B. Fletcher, B. Gras, P. Ewart, C. S. Kim, M. Kim, C. D. Merritt, W. W. Bewley, C. L. Canedy, J. Abell, I. Vurgaftman, and J. R. Meyer, "Mid-infrared multi-mode absorption spectroscopy using interband cascade lasers for multi-species sensing," Opt. Lett. **40**(17), 4186–4189 (2015).

23. C. G. Li, L. Dong, C. T. Zheng, and F. K. Tittel, "Compact TDLAS based optical sensor for ppb-level ethane detection by use of a 3.34 μm room-temperature CW interband cascade laser," Sens. Actuators B Chem. **232**, 188–194 (2016).

24. W. L. Ye, C. T. Zheng, X. Yu, C. X. Zhao, Z. W. Song, and Y. D. Wang, "Design and performances of a mid-infrared CH_4, detection device with novel three-channel-based LS-FTF self-adaptive denoising structure," Sens. Actuators B Chem. **155**(1), 37–45 (2011).

25. R. Arndt, "Analytical line shapes for Lorentzian signals broadened by modulation," J. Appl. Phys. **36**(8), 2522–2524 (1965).

26. S. Haykin, *Adaptive Filter Theory*, 3rd ed. (Prentice Hall Inc., 1995).

27. K. S. Bharath, A. Ara, N. Ramani, K. Bindu, and R. Hegde, "Adaptive Noise Cancellation Filter Using LMS Algorithm on an FPGA for Military Applications," Int. J. Knowl. Eng. **3**, 207–211 (2012).

28. E. Szopos and H. Hedesiu, "LabVIEW FPGA Based Noise Cancelling Using the LMS Adaptive Algorithm," Acta Tech. Napoc. Electron. Telecommun. **50**(4), 5–8 (2009).

29. D. T. M. Slock and T. Kailath, "A fast RLS transversal filter for adaptive linear phase filtering," Int. J. Adapt. Control Signal Process. **2**(3), 157–179 (1988).

30. D. K. K. Saini, "Review of methods of adaptive noise cancellation using LMS and NLMS algorithms," Int. J. Sci. Res. Publ. **2**(6), 99–100 (2012).

31. I. Bamberger, J. Stieger, N. Buchmann, and W. Eugster, "Spatial variability of methane: Attributing atmospheric concentrations to emissions," Environ. Pollut. **190**(190C), 65–74 (2014).

1. Introduction

Methane (CH_4) is the second most important atmospheric greenhouse gas after carbon dioxide (CO_2) [1, 2]. Furthermore as an inflammable and explosive gas, CH_4 is a safety hazard in several industries, such as natural gas production/distribution/storage/transportation, coal

mining, and the handling of liquefied CH_4. Different applications in environmental science, public safety and industrial monitoring have become a driving force for the development of sensitive, accurate, robust and in situ CH_4 sensor systems [3–8]. Compared with conventional mass spectrometry or gas chromatography, infrared laser spectroscopy offers several key advantages in terms of size, time resolution as well as cost and requires no pretreatment and/or accumulation of the concentration of the targeted gas samples, which makes infrared laser spectroscopy particularly suitable for real-time gas sensing applications [9–12].

Tunable laser absorption spectroscopy (TLAS) is a non-contact detection method and has been proven to be an effective tool for trace gas detection [13, 14]. There are two conventional approaches based on the TLAS technique using near- or mid-infrared lasers as infrared excitation sources: wavelength modulation spectroscopy (WMS) [15, 16] and direct laser absorption spectroscopy (DLAS) [17, 18]. An obvious advantage of DLAS is its ability to offer quantitative concentration measurements of trace gas species without calibration as the concentration can be determined from the relative change of the light intensity, which simplifies the sensor structure and signal processing procedure. In order to reduce the limit of detection and to increase detection accuracy, a tunable laser exciting single-frequency laser with a narrow linewidth at the target absorption line of a gas molecule is required for the development of an infrared sensor system. Since most gas molecules have strong absorption in the mid-infrared spectral range, quantum cascade lasers (QCLs) in the 4−12 μm spectral range [19, 20] and interband cascade lasers (ICLs) in the 2.5−6 μm range [21–23] with low power consumption and continuous-wave (CW) output power have become the optimum choice in TLAS applications.

There are many electrical-domain noise sources in a traditional DLAS sensor, which can be generally divided into two categories. Some noise, e.g. White-Gaussian noise generated by electrical components and circuits including detector, data acquisition (DAQ) card and laser driver possess a definite statistical property. However, some noise, e.g. long-term sensor drift and the noise introduced from powerline network possess an unpredictable statistical property. The electrical-domain background noise and interference can be suppressed by either classic hardware-based filters or software-based digital filters. However, potential noise with unpredictable statistical properties cannot be easily suppressed, when the spectral feature of noise falls out of the normal functional spectral range of a classical filter. Compared with a classical filter, a self-adaptive filter can automatically adjust its filtering parameters and therefore achieve the most favorable filtering performance. In 2011, a mid-infrared CH_4 detection sensor system with a novel three-channel-based least square fast transverse filtering (LS-FTF) and a self-adaptive denoising structure was proposed by our group [24], which adopted a novel, additional noise-channel besides the detection- and reference-channels. Different from our previously reported LS-FTF self-adaptive sensor based upon a wideband incandescent lamp and a small-size ellipsoid gas cell/light collector (~7.5 cm), in this paper, the concept of self-adaptive denoising is further extended by means of long-path (16 m) ICL absorption spectroscopy. By incorporating a recursive, least square (RLS) self-adaptive denoising (SAD) algorithm and a 3291 nm ICL, a novel electrical-domain self-adaptive direct laser absorption spectroscopy (SA-DLAS) technique for CH_4 detection is proposed in this work. In addition to the signal channel that delivers the sensing signal from the detector to the data acquisition (DAQ) card, a feedback noise-channel that delivers the ICL drive signal to the DAQ card is created. The noise resulting from the signal generator, current driver electronics and the data sampling module, as well as any power-frequency interference can be obtained and used to self-adaptively denoise the sensing signal with the RLS SAD algorithm. By adding noise into the driving signal of the laser, potential denoising and sensing abilities of the SA-DLAS technique were experimentally evaluated. Sensor performances, including measurement precision and stability were improved by means of the proposed RLS SAD technique. Sensor performance was also evaluated by means of laboratory experiments and indoor/outdoor atmospheric CH_4 measurements.

2. SA-DLAS CH$_4$ sensor configuration

2.1. Sensor architecture

The SA-DLAS CH$_4$ sensor structure is depicted in Fig. 1(a), including both the optical and electrical parts. In the optical part, a Nanoplus CW, thermoelectrically cooled (TEC) ICL was used as the excitation source, which has an operating temperature range of $10 - 20$ °C. A dichroic mirror (DM, ISP Optics, model BSP-DI-25-3) was then used to combine a visible alignment diode laser beam with the mid-infrared ICL beam. The combined beams were coupled to a 16 m multi-pass gas cell (MPGC, physical size: $45 \times 11 \times 11$ cm^3, Egold Technology, Wuhan, Hubei Province, China) using a CaF$_2$ lens (Lens 1, $f = 30$ mm). The lens was placed after the DM to focus the two laser beams into the MPGC to meet the beam pattern-size requirement. The beam entered the gas cell and exited after 36 reflections. The output beam was focused onto a TEC mercury-cadmium-telluride (MCT) photodetector (VIGO System, model PVI-4TE-5) using another lens (Lens 2, $f = 30$ mm). The alignment of the beam was performed at a laboratory temperature (~20 °C) to achieve an absorption path length of 16 m. The cell temperature was not stabilized during the experiment, but was limited within a range of $15 - 30$ °C.
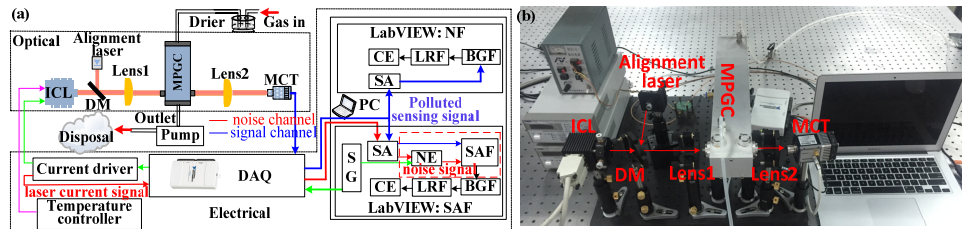

Fig. 1. (a) Schematic of the SA-DLAS CH$_4$ sensor system based on a single CW, TEC ICL. The red line is related to laser current feedback signal (noise channel); The blue line is related to the signal output from the MCT detector (signal channel); The green line is related to the laser drive signal; The pink line represents the signal from the temperature controller. (b) Photograph of the SA-DLAS CH$_4$ sensor system.

The electrical part of the sensor system consists of a laptop (Apple, model # A1466), a DAQ card (National Instrument, model USB-6211), an integrated laser current driver (Thorlabs, LDC210C) and a temperature controller (Thorlabs, TED200C). The ratio between input voltage and output current of the laser driver was adjusted to 5 mA/V by means of an external circuit to improve the current accuracy. A two-channel-based SA-DLAS technique was used for CH$_4$ detection, including both a signal and a noise channel. A scan signal (shown in green color in Fig. 1(a)) was generated by the LabVIEW controlled DAQ card to drive the ICL through the laser current driver. For the signal channel, the MCT detector signal (shown in blue color in Fig. 1(a)) was sent to the DAQ for data acquisition triggered by the signal generation module. For the noise channel, the laser current signal (shown in red color in Fig. 1(a)) generated by the laser current driver (i.e. analog monitoring output "CTL OUT") served as a feedback to the DAQ card for signal acquisition (SA) also triggered by the signal generation (SG) module. A LabVIEW platform was developed for noise extraction (NE), self-adaptive filtering (SAF), background fitting (BGF) and absorption fitting and used to extract the absorption signal for concentration extraction (CE) by means of a self-adaptive RLS algorithm and a Lorenz fitting (LRF) algorithm [25]. Details of the platform are reported in Section 2.5. In addition, a compact, oil-free vacuum pump (KNF Neuberger Inc., model N 813.5 ANE/AF) was used to pump the target gas into the MPGC. Here the gas pressure inside the MPGC without control was equal to ~1 atm during laboratory measurements and field tests. Figure 1(b) shows the photograph of the SA-DLAS CH$_4$ sensor system.

2.2. CH₄ line selection

High-resolution transmission (HITRAN) absorption spectra of 2 parts per million in volume (ppmv) CH_4 and 2% H_2O calculated at 1 atm gas pressure and a 16 m effective optical path length is depicted in Fig. 2, within the wavenumber range of 3036–3042 cm^{-1}. An interference-free CH_4 absorption line centered at 3038.5 cm^{-1} was found and selected as the optimum target line. A H_2O line (~3037 cm^{-1}) was found to be located close to the CH_4 line. In view of the fact that the 3037 cm^{-1} H_2O line is quite flat at ~3038.5 cm^{-1}, the H_2O absorption can be treated as a background signal and its effect can be removed through background elimination. Despite this, a low H_2O concentration, e.g. < 1%, is required to minimize its effect on CH_4 detection, which was realized by using a H_2O trap based on calcium sulfate (W.A. Hammond Drierite, CAS# 7778-18-9). Generally, the drier can reduce the H_2O concentration to < 0.1%. Hence a change of the H_2O concentration level within 0 − 0.1% will cause no effect on the CH_4 detection. The drier needs to be replaced periodically for long-term measurements to ensure a relative H_2O concentration of < 0.1%.
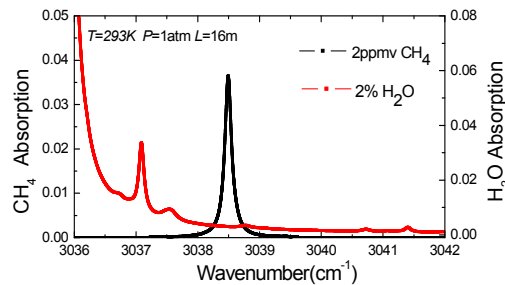

Fig. 2. HITRAN based absorption spectra of CH_4 (2 ppmv) and H_2O (2%) in a narrow spectral range from 3036 cm^{-1} to 3042 cm^{-1} at a pressure of 1 atm and an absorption length of 16 m. CH_4 and H_2O lines are shown in black and red, respectively.

2.3. ICL and MCT detector characterization

The ICL has a center wavelength of 3.291 μm in order to target the selected CH_4 absorption line. The physical size of the TO66-mounted ICL is $5 \times 5 \times 5$ cm^3, which can be operated at a temperature between 10 °C and 20°C without forced air or water cooling. An infrared power meter (Ophir, model 3A) was used to measure the ICL emission power at different driving currents at 15°C, as shown in Fig. 3(a). A Fourier transform infrared (FTIR) spectrometer (Thermo Fisher Scientific, model Nicolet iS50) was employed to measure the ICL emission spectrum, as shown in Fig. 3(b). Figure 3(c) shows that the emission wavenumber can be tuned from 3035.5 cm^{-1} to 3042.1 cm^{-1} for different temperatures and driving currents. The current and temperature tuning coefficient for this ICL were measured to be − 0.1593 cm^{-1}/mA and − 0.3051 cm^{-1}/°C, respectively. An ICL drive current of 52 mA and an operating temperature of 15°C were selected for targeting the interference-free absorption line of 3038.5 cm^{-1} in CH_4 concentration measurements.

A TEC MCT photodetector (VIGO System, model PVI-4TE-5), which is available in TO-8 package with a BaF_2 window, was selected to measure the power of the output beam with CH_4 absorption. The active area of the detector is 1×1 mm^2. The 3 dB cutoff frequency without bias of the detector is > 15 MHz. At an optimal wavelength of 5 μm, the detectivity and responsivity of the MCT detector are ~1.2×10^{11} $cmHz^{1/2}$/W and ~2.1 A/W, respectively.
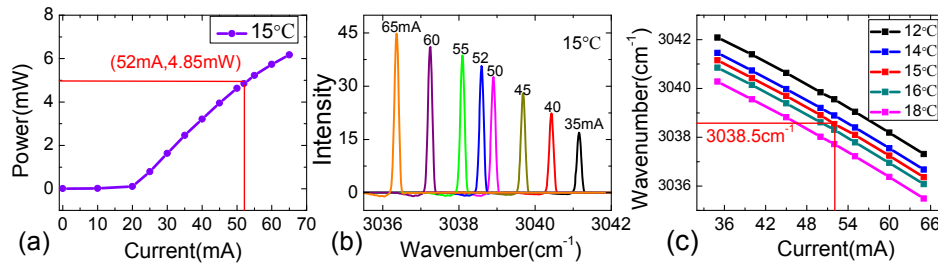
Fig. 3. (a) The measured output power for the 3.291 μm CW TEC ICL at different drive current at 15 °C. (b) The measured ICL emission spectrum for the 3.291μm CW TEC ICL under an operating temperature of 15°C. (c) Curves of emission wavenumber versus ICL temperature and drive current.
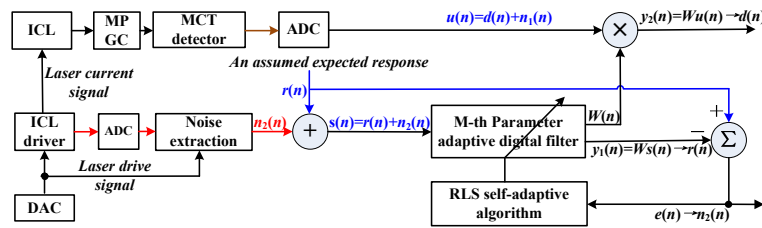

Fig. 4. RLS-based SAD principle used in the SA-DLAS CH₄ sensor, where $u(n)$ is the output from the detector, $n_2(n)$ is the noise extracted from the feedback of the laser drive signal.

2.4. RLS SAD algorithm for DLAS signal processing

The RLS denoising algorithm is a self-adaptive modern filtering algorithm, which has a faster rate of convergence compared with the least mean square (LMS) algorithm [26–30]. A self-adaptive filter can adjust its weighting coefficients automatically and estimate the statistic properties of both signal and noise to achieve the best filtering results. The universal RLS denoising principle to be used in the SA-DLAS CH₄ sensor is shown in Fig. 4, which comprises two needed input channels. For the signal-channel, the sensing signal $u(n)$ from the MCT detector contains not only a pure signal $d(n)$ but also a noise signal $n_1(n)$; For the noise-channel, there is only a noise signal $n_2(n)$ that is obtained through noise extraction from the feedback signal of the ICL driver. It should be noted that $n_1(n)$ and $n_2(n)$ induced by the laser driver and DAQ card are not equal but are of the same statistical property, which means that $n_1(n)$ can be expressed by a nonlinear weighting transformation on $n_2(n)$. $r(n)$ is an assumed expected output, which is only used for the optimization of weighting coefficients. $y_1(n)$ is the output signal from the M-th parameter-adjustable digital filter, which is the weighting transformation on $s(n)$. $e(n)$ is the error output of the self-adaptive filter, which is the subtraction between $r(n)$ and $y_1(n)$. By adjusting the weighting coefficient vector $\mathbf{W}(n)$, $y_1(n)$ can gradually approach $r(n)$. With the tap-weight vector $\mathbf{W}(n)$, it is feasible to train the input signal $u(n)$ and finally obtain the best filtering result $y_2(n)$, i.e. the best estimation of $d(n)$.

The formulations are deduced as described below. Since n_1 is correlated with n_2, n_1 can be expressed as the linear weighting sum form of n_2, and d is uncorrelated with n_1 and n_2. According to Fig. 4, the error output $e(n)$ is

$$e(n) = r(n) - y_1(n) = r(n) - \mathbf{W}^H(n-1)\mathbf{s}(n) \tag{1}$$

Then we define a cost function $\xi(n)$, as

$$\xi(n) = \sum_{i=1}^{n} \lambda^{n-i} |e(i)|^2 \tag{2}$$

where λ is a forgetting factor, i.e. a positive constant close to, but < 1. Our target is to achieve the optimum value of the tap-weight vector $\mathbf{W}(n)$ to ensure that the cost function $\xi(n)$ attains its minimum value. The best $\mathbf{W}(n)$ can be written as

$$\mathbf{\Phi}(n)\mathbf{W}(n) = \mathbf{\varphi}(n) \tag{3}$$

where the $M \times M$ correlation matrix $\mathbf{\Phi}(n)$ is defined as

$$\mathbf{\Phi}(n) = \sum_{i=1}^{n} \lambda^{n-i}\mathbf{s}(i)\mathbf{s}^{H}(i) \tag{4}$$

The $M \times 1$ cross-correlation vector $\mathbf{\varphi}(n)$ between the tap inputs of the transversal filter and the desired response is correspondingly defined by

$$\mathbf{\varphi}(n) = \sum_{i=1}^{n} \lambda^{n-i}\mathbf{s}(i)r^{*}(i) \tag{5}$$

$$\mathbf{\Phi}^{-1}(n) = \lambda^{-1}\mathbf{\Phi}^{-1}(n-1) - \frac{\lambda^{-2}\mathbf{\Phi}^{-1}(n-1)\mathbf{s}(n)\mathbf{s}^{H}(n)\mathbf{\Phi}^{-1}(n-1)}{1+\lambda^{-1}\mathbf{s}^{H}(n)\mathbf{\Phi}^{-1}(n-1)\mathbf{s}(n)} \tag{6}$$

Therefore, Eq. (3) can be expressed as

$$\mathbf{W}(n) = \mathbf{\Phi}^{-1}(n)\mathbf{\varphi}(n) \tag{7}$$

For computational convenience, let

$$\mathbf{P}(n) = \mathbf{\Phi}^{-1}(n) \tag{8}$$

$$\mathbf{k}(n) = \frac{\lambda^{-1}\mathbf{P}(n-1)\mathbf{s}(n)}{1+\lambda^{-1}\mathbf{s}^{H}(n)\mathbf{P}(n-1)\mathbf{s}(n)} \tag{9}$$

Using these definitions, we may rewrite Eq. (7) as follows

$$\begin{aligned}
\mathbf{W}(n) = \mathbf{\Phi}^{-1}(n)\mathbf{\varphi}(n) &= \mathbf{W}(n-1) + \mathbf{k}(n) \\
&= \mathbf{W}(n-1) + \mathbf{k}(n)e^{*}(n)\left[r^{*}(n) - \mathbf{s}^{H}(n)\mathbf{W}(n-1)\right] \\
&= \mathbf{W}(n-1) + \mathbf{k}(n)e^{*}(n)
\end{aligned} \tag{10}$$

Hence we can summarize the RLS algorithm as follows:

Step 1: Initialize the algorithm. Assign a known expected output $\mathbf{r}$. Define δ as a small positive constant and $\mathbf{I}$ is a unit vector. Let $\mathbf{W}(0) = \mathbf{0}$, and $\mathbf{P}(0) = \delta^{-1}\mathbf{I}$.

Step 2: Perform iterative calculations for M times. Calculate $y_1(n)$ and $e(n)$, update the gain $\mathbf{k}(n)$ and the weight vector $\mathbf{W}(n)$, and the inverse matrix $\mathbf{P}(n)$. Finally, we obtain an optimized weighting coefficient $\mathbf{W}$.

Step 3: Use the optimum tap-weight vector $\mathbf{W}$ to denoise the sensing signal $\boldsymbol{u}$.

According to the above denoising principle of RLS algorithm, a simulation program based on MATLAB was compiled for which the function prototype is

$$function[e, y_2] = RLS\_algorithm(M, \lambda, u, n_2) \tag{11}$$

The definitions of related parameters in the program are the same as those in Eqs. (1)-(10).

For a DLAS sensor, there is a decrease of $u(t)$ due to gas absorption relative to the background signal $u_{bac}(t)$, which can be obtained from background fitting. Then the normalized absorbance can be expressed as $u_{absorbance}(t) = -\ln(u(t)/u_{bac}(t))$. Three typical noise,

low-frequency (near to the scan frequency of the laser), high-frequency (much larger than the scan frequency) and White-Gaussian noise were introduced in the numerical simulation to evaluate the filtering performance of the RLS SAD algorithm. Let $d(t)$ be a simulated absorption signal of CH_4 based on the HITRAN 2012 database ($P = 760$ Torr, $T = 293$ K, $L = 16$ m, $C = 2.0$ ppmv) with a variation range from ~1.5 V to ~1.9 V. Figures 5(a) and 5(b) show the denoising simulation based on MATLAB platform on the polluted 1 Hz absorption signal (where only the first half of the triangular signal (~0.5 s) was used to extract the absorbance) $u(t) = d(t) + n_1(t)$ by a low-frequency noise, represented by $n_1(t) = n_2(t) = 0.05\cos(60\pi t)$ V corresponding to a frequency of 30 Hz and a noise level (i.e. amplitude) of 50 mV, where $M = 100$ and $\lambda = 0.9$. The sub-figures show the un-denoised and denoised absorbance curves. It can be found that all the added noise are removed and the denoised signal can approach to the pure signal d. Similar denoising results can be obtained using RLS SAD when high-frequency noise (frequency: 60 kHz; noise level: 50 mV) and White-Gaussian noise (noise level represented by standard deviation: 50 mV) were applied on $d(t)$. These simulations confirm the normal denoising operation of the RLS SAD algorithm. Notice that the defined noise level is the noise strength relative to the MCT detector's output and not the laser drive signal.
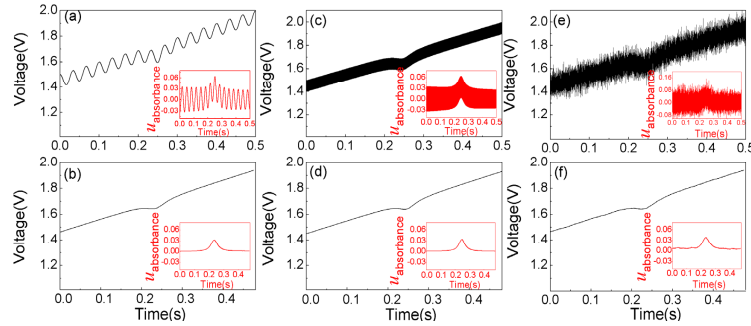

Fig. 5. Denoising simulation on (a) the polluted absorption signal $u(t) = d(t) + n_1(t)$ by a low-frequency noise signal, where $n_1(t) = n_2(t) = 0.05\cos(60\pi t)$ V, (b) the denoised output from the RLS self-adaptive filter; Denoising simulation on (c) the polluted absorption signal $u(t) = d(t) + n_1(t)$ by a high-frequency noise signal, where $n_1(t) = n_2(t) = 0.05\cos(120000\pi t)$ V, (d) the denoised output from the RLS self-adaptive filter; Denoising simulation on (e) the polluted absorption signal $u(t) = d(t) + n_1(t)$ by a White-Gaussian noise with a standard deviation of 0.05 V, and (f) the denoised output from the RLS self-adaptive filter. The sub-graphs are the corresponding normalized absorbance curves for the three cases, respectively.

In addition, the effects of each parameter on the filtering performance are determined to be: (1) the convergence speed decreases as M increases; (2) the inverse of $1 - \lambda$ represents the algorithm memory. When the filter operates in a nonstationary environment, λ should be decreased to ensure that the past data are disregarded and follow the new statistical variations.

2.5. LabVIEW-based SA-DLAS platform

In order to remove sensing noise using the RLS SAD algorithm, a LabVIEW-based laptop platform was developed, whose function diagram is shown in Fig. 6. There are four main functions in this platform, involving SG, SA, SAF, and CE. For SG, a scan-signal array was generated to modulate the laser driver. The generated noise signal array was selected and superimposed on the scan-signal for the verification of the SA-DLAS technique (See Sections 3.1). The drive signal was supplied to the ICL via the digital-to-analog converter (DAC) module of the DAQ card. For SA, via the use of an analog-to-digital converter (ADC), the output signal from the MCT detector and the laser current feedback signal from the laser driver were sampled at the same sampling rate with the DAC. A noise signal was obtained via the subtraction between the sampled feedback signal and the generated laser drive signal. For

SAF, the noise signal and sensing signal were sent to the RLS-based self-adaptive filter for noise suppression. For CE, with the denoised signal, by using background fitting and Lorenz fitting, the normalized absorbance i.e. $-\ln(u(t)/u_{bac}(t))$ was extracted to determine CH_4 concentration levels. The procedure of fitting a Lorentzian lineshape can effectively reduce both regular noise (e.g. White-Gaussian noise) and shot spike noise. However, if the sensing signal is affected by irregular noise, e.g. a low-frequency drift, resulting in the position or amplitude change of the absorption peak or some non-absorption peaks in the absorption signal, the Lorentzian fitting will not function normally. In order to obtain an accurate Lorentzian lineshape, we first use the SAF method to denoise such kind of noise and then use the Lorentzian fitting to further reduce the residual noise.
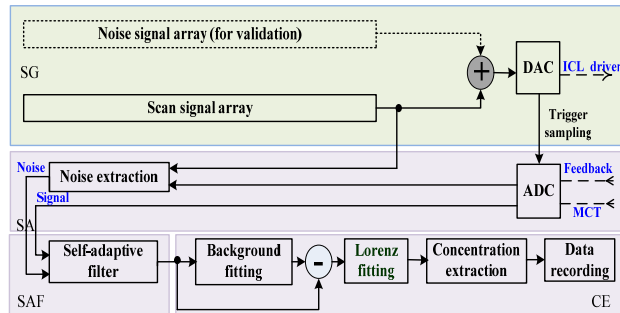
Fig. 6. Function diagram of the LabVIEW-based laptop platform, which performs four functions including SG, SA, SAF and CE.

3. SA-DLAS CH$_4$ Sensor performances

For targeting the CH_4 absorption line at 3038.5 cm^{-1}, the ICL drive current and temperature, as well as the pressure without control in the MPGC were set to 52 mA, 15°C and ~1 atm, respectively. The scan signal was a triangular signal with a frequency of 1 Hz and a peak-to-peak amplitude of 1.64 V. The sampling rate of the ADC module in DAQ card was set to 2 kHz, resulting in 2000 data points per triangular period. Sync sampling was realized by using the scan signal of the laser as a trigger signal. Only the first 1000 data points were sampled for the first half of a triangular period of ~0.5 s and sent to the signal-processing module. The needed processing time with the denoising algorithm, dependent on the number of the sampled data dots per half triangular period, was ~5.5 s, leading to a sampling period of ~6 s plus the data acquisition time.

3.1. Filtering performances using two signal-processing schemes

As a comparison, two signal-processing schemes were used in the DLAS sensor by pumping a 2-ppmv CH_4 sample into the MPGC, including no filtering (NF) and SAF (Fig. 1(a)). Different kinds of noise were superimposed on the laser scan signal, generating a noise background in the ICL emission light power and wavelength. Figures 7(a)-7(c) show the measured output signal from the MCT detector, where (a) a low-frequency noise $(0.1\cos(60\pi t)$ V), (b) a high-frequency noise $(0.15\cos(120000\pi t)$ V) and (c) a White-Gaussian noise (standard deviation is 0.15 V) were imposed on the scan signal, respectively. Figures 7(e)-7(g) show the absorbance using NF and using SAF. The red curves are the denoised absorbance using a RLS-based self-adaptive filter. Figure 7(d) is the output signal from the MCT detector when a composite noise signal, i.e. a low-frequency noise $0.1\cos(60\pi t)$ V, a high-frequency noise $0.05\cos(120000\pi t)$ V and a White-Gaussian noise (standard deviation is 0.08 V)) were merged and imposed on the laser scan signal. As shown in Fig. 7(h), if no filter was used during detection, the absorbance curves contain too many noise to be processed for concentration extraction, leading to poor accuracy and stability. The proposed SAF can deal with any kind of noise and thus improve the sensor performance, indicating an obvious

advantage over the classic filtering method. It was found through experiment that, as the high- and low-frequency noise level increases, the denoising performance initially decreases and then improves, indicating that there is a worst noise level for these two noise levels. Compared to high- and low-frequency noise, the effect of White-Gaussian noise differs, and the larger the noise level, the poorer the sensor performance.
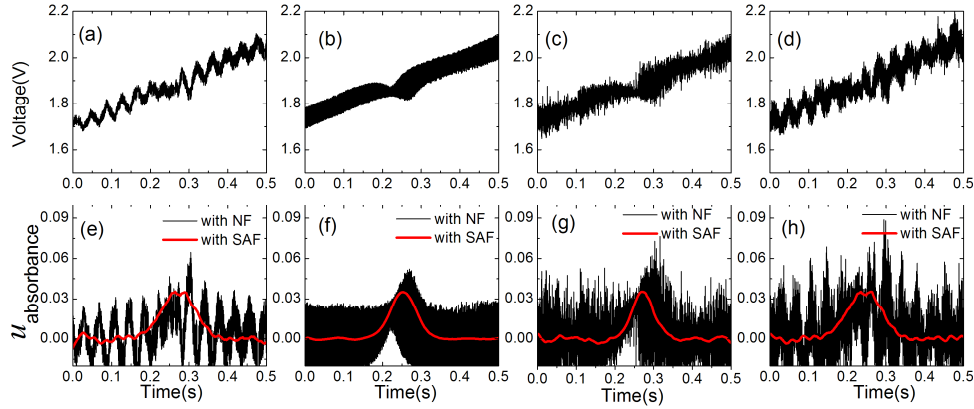

Fig. 7. Measured MCT output signals when (a) a 30 Hz low-frequency noise with an equivalent noise level of 25 mV, (b) a 60 kHz high-frequency noise with an equivalent noise level of 37.5 mV, (c) a White-Gaussian noise with an equivalent noise level (standard deviation) of 37.5 mV, and (d) a composite noise was imposed on the laser scan signal; (e)-(h) are the calculated normalized absorbance curves using NF and using SAF under the four noise cases shown in (a), (b), (c) and (d), respectively.
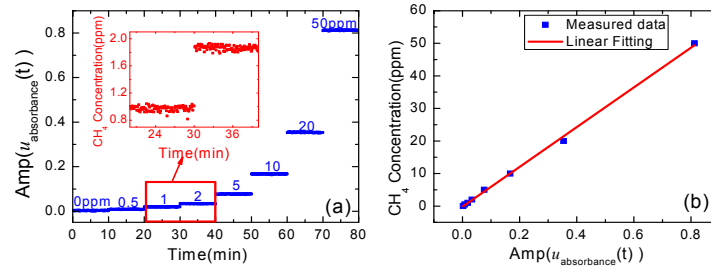

Fig. 8. (a) Measured amplitude of $u_{absorbance}(t)$ versus calibration time t for eight CH_4 concentration levels of 0, 0.5, 1, 2, 5, 10, 20, 50 ppmv. The inset in Fig. 8(a) shows the fluctuation of the measured CH_4 results at 1 ppmv and 2 ppmv concentration levels; (b) Experimental data dots and fitting curve of CH_4 concentration versus the amplitude of $u_{absorbance}(t)$.

3.2. Calibration and data-fitting

With the SAF algorithm, CH_4 sensor calibration was carried out by using diluted standard CH_4 gas samples with eight concentration levels of 0, 0.5, 1, 2, 5, 10, 20 and 50 ppmv. The amplitude of the normalized absorbance signal ($u_{absorbance}(t) = -\ln(u(t)/u_{bac}(t))$) was recorded for ~10 min for each concentration, as shown in Fig. 8(a). The measured amplitude for each concentration was then averaged and plotted as a function of CH_4 concentration, as shown in Fig. 8(b). A linear relation was observed between the amplitude of the absorbance signal and the concentration, given by:

$$C = 61.09118 \times \text{Amp}\left(u_{absorbance}\left(t\right)\right) - 0.19545 \qquad (12)$$

The fitting curve indicates a good linear relationship (R-square value: 99.84%) between the amplitude of the absorbance signal and CH_4 concentration. With the measured amplitude of

the absorbance signal, Eq. (12) was used to determine CH_4 concentration levels. However, as can be seen from Eq. (12), due to some residual noise in the sensor system, a non-zero absorbance value is obtained even though the concentration is zero.

3.3. Sensor stability

Without external applied noises, the intrinsic noise level of the SA-DLAS sensor system was determined by passing pure N_2 into the gas cell and the subsequent monitoring of normalized absorbance. The absorbance can be transformed to CH_4 concentration based on their relationship. CH_4 concentration measurements of the sample with zero concentration were performed over a time period of ~45 min as shown in Fig. 9. In Fig. 9(a), the total variation range of the measured concentration is ~−197–255 ppbv for the 45-min observation time without filtering. The Allan deviation was plotted on a log-log scale versus the averaging time, τ. The plot indicates a measurement precision of ~78.8 ppbv with a ~6 s averaging time. With increasing averaging time, a measurement precision of ~11.6 ppbv with a ~288 s averaging time was obtained. As shown in Fig. 9(b), with SAF, the total variation range of the measured concentration is ~−117–124 ppbv and a measurement precision of ~43.9 ppbv with a ~6 s averaging time and 6.3 ppbv with a ~240 s averaging time were obtained. Hence the SA-DLAS technique is useful in suppressing the intrinsic noise (i.e. a low noise level in an ideal laboratory environment) of the sensor. Since the simulated noise levels in Figs. 5 and 7 are much larger than the intrinsic level in Fig. 9, the denoising performance shown in Fig. 9 is not as obvious as those in Figs. 5 and 7. However, the decrease of Allan deviation indicates a favorable noise suppression ability of the SA-DLAS technique as we compare Fig. 9(a) with Fig. 9(b). Additionally, the Allan deviation plot for the two cases stops decreasing nearly at a similar acquisition time, since the two measurement schemes are based on the same hardware platform.
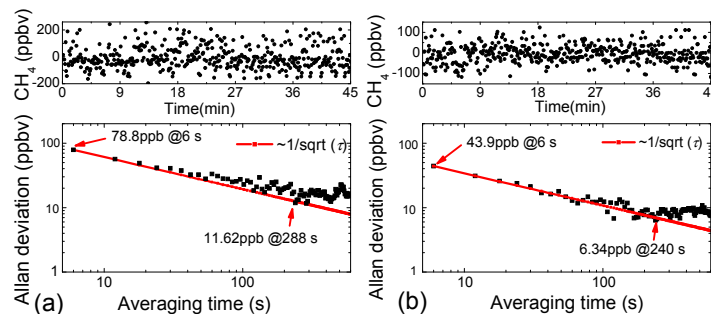

Fig. 9. (a) Allan-Werle deviation plot using NF as a function of averaging time, τ, based on the data shown in the upper figure; (b) Allan-Werle deviation plot using SAF as a function of averaging time, τ, based on the data shown in the upper figures.

3.4. Sensor dynamic response

In the measurement of dynamic response, two valves were used to switch between the two gas streams into the MPGC, as shown in Fig. 10(a). A 'Y' connector with two entrance ports and one exit port was selected. One entrance port was connected to a standard 2 ppmv CH_4 sample, and the other one was connected to a pure N_2 cylinder. The exit port was connected to the MPGC. The two entrance ports could be switched "on" or "off" by two needle valves for the dynamic tests. The measurement results are shown in Fig. 10(b). Under a gas flow rate of ~500 ml/min, a 10–90% rise time of ~54 s and a 90–10% fall time of 48 s were determined, respectively.
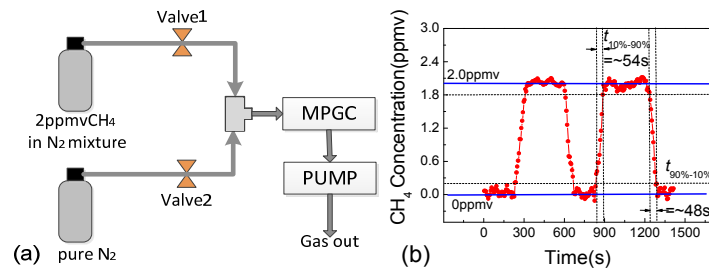
Fig. 10. (a) Schematic of a vacuum 'Y' connector with two entrance ports and one exit port. (b) Response time measurement results by varying CH_4 concentration between 0 and 2 ppmv.

4. Atmospheric CH_4 measurements with/without SAF

4.1. Indoor CH_4 measurements

The sensor system was evaluated for CH_4 concentration measurements in a laboratory environment (in the Infrared Opto-Electron Application Laboratory at Jilin University). Measured CH_4 concentration levels from 22:00 pm, June 21, 2017 to 10:00 am, June 23, 2017, Beijing Time) are displayed in Fig. 11(a). It is observed that the measured CH_4 concentrations during this period of time show an average of ~2.012 ppm ± 147.49 ppbv (1σ) using NF, and show an average of ~1.998 ppm ± 149.15ppbv (1σ) using the SAF technique. The CH_4 concentration exhibited relatively minor variations during the period of monitoring (relative standard deviation ~7.5%), with a slight increase during the early morning hours followed by decreasing concentrations during the day as observed in previous studies [31].
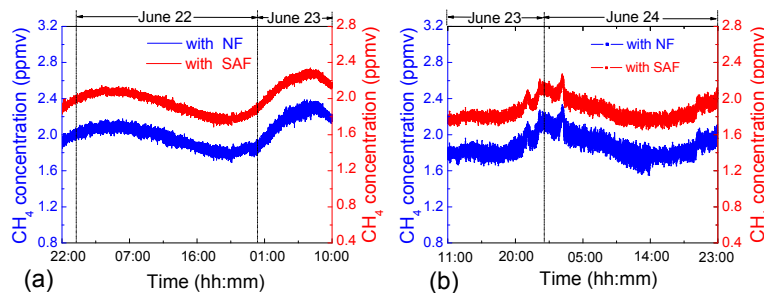

Fig. 11. (a) Measured concentration of CH_4 in ambient air during ~36 hours period on June 21-23, 2017 inside the Infrared Opto-Electron Application Laboratory (located in the D part, Tang Aoqing building, Jilin University). (b) Measurement results of CH_4 monitoring in the atmosphere for ~36 hours time duration on the Jilin University campus. The red curve is the measured concentration with SAF and the blue curve is the measured concentration using NF.

4.2. Outdoor measurements

The sensor system was also evaluated for detection of atmospheric CH_4 on the Jilin University campus. For continuous day and night outdoor monitoring, the sensor was placed inside the laboratory and the outside air was pumped into the gas cell using a long sampling line. The measured concentrations are plotted in Fig. 11(b). These experiments were conducted from 11:00 am on Jun 23, 2017 to 23:00 pm on June 24, 2017 (~36 hours sampling), Beijing time. Fluctuations in concentration levels were observed during atmospheric monitoring of CH_4. CH_4 concentrations were above 2 ppmv during the early morning hours and then dropped gradually to its typical urban background level of ~1.81 ppmv. When using SAF and using NF, the measured concentration shows an average value of ~1.870 ppm ± 109.41 ppbv (1σ) and ~1.876 ppm ± 123.38 ppbv (1σ), respectively. The detected CH_4 concentration levels exhibited a typical hourly profile expected for this gas species, which is related to boundary layer dynamics and the extent of mixing in the

atmosphere [31]. An offset between NF and SAF is observed for indoor and outdoor CH_4 measurements. An explanation for this offset is that the fitting equation (Eq. (12)), which was derived from the sensor calibration using the SAF scheme, was used to calculate the CH_4 concentration for the two schemes. Since the simulated noise levels in Figs. 5 and 7 are much larger than the intrinsic level in Fig. 11, the denoising performance in Fig. 11 is not as obvious as those in Figs. 5 and 7. However, the decrease of Allan deviation indicates a noise suppression effect by using the SA-DLAS technique.

5. Conclusions

In order to suppress the potential noise with unpredictable statistical properties, a novel SA-DLAS CH_4 sensor architecture was proposed by incorporating a CW DFB ICL and a RLS SAD algorithm. Both numerical simulations and experiments were carried out to verify the SA-DLAS sensor performance by imposing low-frequency noise, high-frequency noise, White-Gaussian noise, and hybrid noise on the laser scan signal. Two measurement schemes (without and with SAF) were employed to assess the CH_4 sensor performance. Only considering the intrinsic sensor noise, the measurement precision was decreased from ~78.8 ppbv (@6 s) to ~43.9 ppbv (@6 s) via the use of SAF. Dynamic measurements of the sensor system indicate a 10–90% rise time of 54 s and a 90–10% fall time of ~48 s. Indoor and outdoor atmospheric CH_4 measurements were conducted to evaluate the field sensor performance. The demonstrated SA-DLAS sensor architecture shows the merits of suppression of potential noise with unpredictable statistical properties, which is also suitable for other infrared gas sensing applications.

Funding